

Experimental and Computational Study of Area Printing™ Additive Manufacturing: Inconel 718 and M300 Maraging Steel Density Improvement

B. Fotovvati, S. Shrestha, N. Ferreri, and N. Duanmu

Seurat Technologies Inc., Wilmington, MA, USA 01887

Abstract

The low manufacturing speed of laser-powder bed fusion (LPBF) additive manufacturing has hindered its adoption in conventional manufacturing methods. Large-area pulsed laser powder bed fusion (LAPBF), also known as "Area Printing™", has addressed this limitation by replacing the point laser with a large-area pulsed laser. Each pulse melts a region of the powder bed in the order of square millimeters, which enables scalability without the sacrifice of resolution and high throughput at an equivalent or better quality (in part due to a lack of spatter) when compared to conventional LPBF methods. In this study, process parameters are optimized to achieve near-full-density parts, and a computational model is developed to understand the multi-physics governing the process. It is observed that the shallow depth and high aspect ratio of the melt pool lead to a unidirectional solidification front extending along the build direction where grains grow epitaxially, and highly directional microstructures are created.

Keywords: Selective Laser Melting; Area Printing™; Thermo-fluid Modeling; Inconel 718; M300 Maraging Steel

1. Introduction

Laser-based powder bed fusion (LPBF), also known as selective laser melting (SLM), or direct metal laser sintering (DMLS), is one of the most popular types of metal additive manufacturing (AM). LPBF employs metal powders selectively melted in a layer-wise manner using a high-intensity laser beam in correspondence with a sliced, computer-aided design (CAD) model. LPBF is widely used in various industries, including medical, automotive, and aerospace. Some examples of these applications include patient-specific metal implants [1], turbine blades [2], engine manifolds [3], and lattice structures [4]. The popularity of this manufacturing technique in such industries is due to the many advantages that this method offers: design freedom, reduced manufacturing time, minimized material waste, sustainability benefits, etc. [5]. However, LPBF's low production rate coupled with the typical capital and operational costs, has limited its adoption over conventional manufacturing methods. To address this challenge, Seurat Technologies has developed large-area pulsed laser powder bed fusion (LAPBF), also known as "Area Printing™," which replaces the point laser in conventional LPBF with a large-area pulsed laser. LAPBF melts on the scale of several millimeters in a single pulse with a repetition speed of up to 40 Hz. This can result in significantly shorter manufacturing times and lower final production costs. The large-area laser beam also minimizes spattering issues commonly encountered in the conventional LPBF process, as there is no deep turbulent melt pool to create strong recoil pressures and eject particles.

Several studies have investigated the effect of laser parameters, such as laser power and scan speed, on the quality and properties of LPBF-fabricated parts. Research studies show changing laser power and scanning speed have different effects on pore formation in IN718 [6,7]. Additionally, Wang et al. [8] optimized the LPBF process parameters to get high-density IN718 samples and investigated the effects of heat treatments on microstructure and mechanical properties. Using a laser power of 150 W, a scanning speed of 550 mm/s, and a 45 % overlap rate (yielding an energy density of 158 J/mm³), they achieved a relative density of 99.8%. Liu et al. [9] explored the effects of the LPBF process parameters on the microstructure of IN718 samples and observed that as the energy density decreases, the aspect ratio of the columnar grains becomes lower due to insufficient epitaxial growth. They concluded that refined grains appeared due to the relatively fast solidification occurring in the relatively shallow melt pool. Georgilas et al. [10] investigated the effects of laser power and exposure time on the density of IN718 samples fabricated by pulsed LPBF. They achieved a maximum relative density of 99.8% with laser power of 200 W and exposure time of 110 μs. The grain structure of the as-built pulsed LPBF IN718 material was less directional (morphologically and crystallographically) than continuous LPBF.

There is little work in the literature on the additive manufacturing of maraging steels. M300 and 18Ni300 are among the most popular maraging steels in the AM industry. Due to their excellent combination of strength and fracture toughness, maraging steels are mainly used in the tool and aerospace industries. Their very low carbon content gives them excellent weldability and high toughness [11]. Casalino et al. [12] showed that relative densities higher than 99.0% could be achieved for 18Ni300 maraging steel in the LPBF process by using laser powers higher than 90 W and a scanning speed lower than 220 mm/s. They also demonstrated that the hardness, the mechanical strength, and the surface roughness correlated positively to the part density. Krol et al. [13] investigated the effects of LPBF process parameters on the density of 18Ni300 maraging steel and achieved 99.3 % relative density with 200 W of laser power and a scanning speed of 340 mm/s.

Mao et al. [14] used a relational model between the LPBF process parameters and the relative density of 18Ni300 maraging steel samples to obtain a relative density of 99.5% using laser power of 284 W and a scanning speed of 868 mm/s. Vishwakarma et al. [15] studied the effect of build orientation on the microstructure and tensile behavior of LPBF-fabricated M300 maraging steel and achieved 99.6 % relative density using a laser energy density of 62.5 J/mm³. Fine grains with an average size of ~0.31 μm were observed in their as-built samples.

In this study, the parameter optimization of the LAPBF process is presented to achieve near-full-density (>99.9 % relative density) parts using two popular metallic materials: Ni-based superalloy 718 (IN718) and M300 maraging steel. The aim is to obtain high-density parts. Additionally, a computational model is developed to better understand the underlying physics of the process, including thermal dynamics, fluid flow, and phase transformations, to provide insights into the relationship between process parameters and part quality. Overall, this study aims to contribute to developing high-quality, cost-effective AM processes using LAPBF, which could have significant implications for various industrial sectors.

2. Methodologies

2.1. Experimental methods

In Area PrintingTM, a laser containing millions of pixels is utilized to melt metal powder layers and fuse them to the area below it, manufacturing entire renderings at once in a single defined area. A set of diode lasers are used to preheat the powder bed before a single Nd:YAG pulsed laser performs the final melting of the area. Figure 1 illustrates a schematic of the pulsed laser beam from the source to the powder bed. Once the laser is created, it is shaped into a homogeneous square field called a "tile". A blue light projector then generates a projection of the area pattern the same size as the square laser beam, which is aligned with the laser beam. An optically addressable light valve (OALV) receives this light and horizontally polarizes the laser beam where blue and IR light pixels overlap and vertically polarizes them where they do not overlap. The vertically and horizontally polarized laser beams are then split, and the resulting area pattern is sent through a scanner system to the powder bed to melt the patterned field.

IN718 and M300 maraging steel powders with particle size distributions of 15–37 μm and 15–45 μm , respectively, were used for the experiments. Each density-optimization print job contained a seven-by-seven grid of 10 mm x 10 mm x 10 mm density cubes on an Area PrintingTM Prototype System. After print completion, the build plate was taken out, and the samples were cut from the build plate using a horizontal band saw. The samples were then soaked in isopropanol in an ultrasonic cleaner for 30 minutes removal for density measurements. The density measurements are performed using the Archimedes method and an Ohaus ExplorerTM Precision density kit. Micrographs were taken using an Olympus LEXTTM OLS5100 3D laser scanning microscope and processed using an in-house developed code for defect classification.

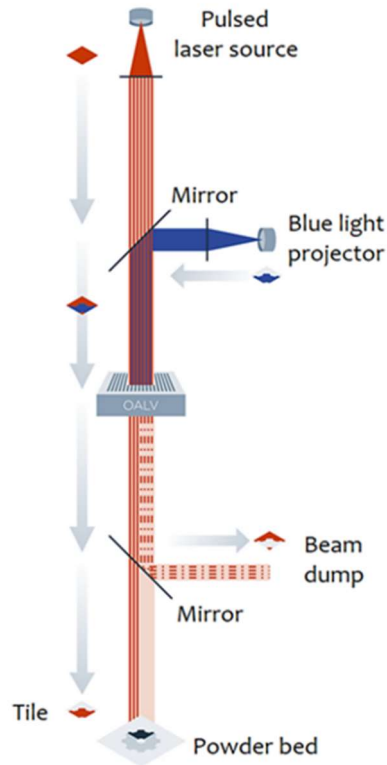


Figure 1. Schematic of the pulsed laser beam used in the Area Printing™ process [16].

2.2. Computational methods

The integrated LPBF process simulation was implemented based on two steps: powder deposition using the discrete element method (DEM) and laser-powder interaction using computational fluid dynamics (CFD). The powder deposition was modeled using the open-source DEM code LIGGGHTS (LAMMPS Improved for General Granular and Granular Heat Transfer Simulations) [17]. The material properties of IN718 used in the DEM simulation were density of 8.17 g/ml, modulus of elasticity of 20 MPa, Poisson's ratio of 0.29, sliding friction coefficients of 0.4, rolling friction coefficient of 0.1, and coefficient of restitution of 0.4.

After the powder bed was obtained from the DEM simulation, it was saved as a Stereolithography (STL) file and imported to Flow-3D software version 11.2.6.4 (Flow Science, Inc., Santa Fe, New Mexico, USA). The governing equations of DEM and CFD are explained in our previous work [18,19]. Temperature-dependent material properties such as density, specific heat, thermal conductivity, and viscosity are used [20].

Figure 2 shows the computational domain and dimensions. In this model, the powder particles are contactless or have minimal contact to increase the accuracy of slow powder bed heating with diodes. Hence, the mesh size varies from 1.2 μm to 5 μm in the powder region. Due to the lower mesh size, a laser illumination area of 0.3 mm \times 0.3 mm was used to run the simulation in a reasonable time.

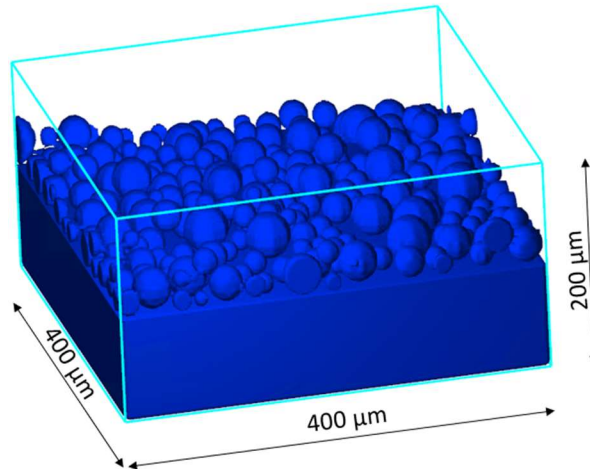


Figure 2. Computational model of the powder bed.

3. Results and Discussions

The results of the experiments and simulations are presented and discussed in the following sub-sections.

3.1. Experimental results

3.1.1. Effect of Laser Energy Density on Relative Density

The observed effect of diode laser fluence on the porosity of area printed density cubes is presented in Figure 3. The relationship amongst diode laser flux, pulse length, and porosity is illustrated in Figure 4 and constitutes a regression of the experimental data. The domain on each plot in Figure 3 and Figure 4 is divided into different regions based on the observed defect type. Notably, the near-full-density area for IN718 is significantly narrower than that of M300. The observed behavior for IN718 aligns with what is reported in the literature [21]. This is due to IN718 being prone to internal cracking at high energy densities [22]. No inflection point was observed in the porosity plot of M300 samples by increasing the applied energy density. More experiments at higher energy densities and comparing the fully dense samples at various energies are yet to be carried out. Figure 5 and Figure 6 illustrate representative micrographs of samples of each material fabricated using the parameters corresponding to different regions. As seen in Figure 5-c, most cracks are oriented in the build direction, categorizing them as hot cracking or hydrogen embrittlement [23]. A deeper investigation into crack morphology and distribution, local solute composition, and precipitation around the crack is required to confirm the crack types observed in the IN718 microstructure.

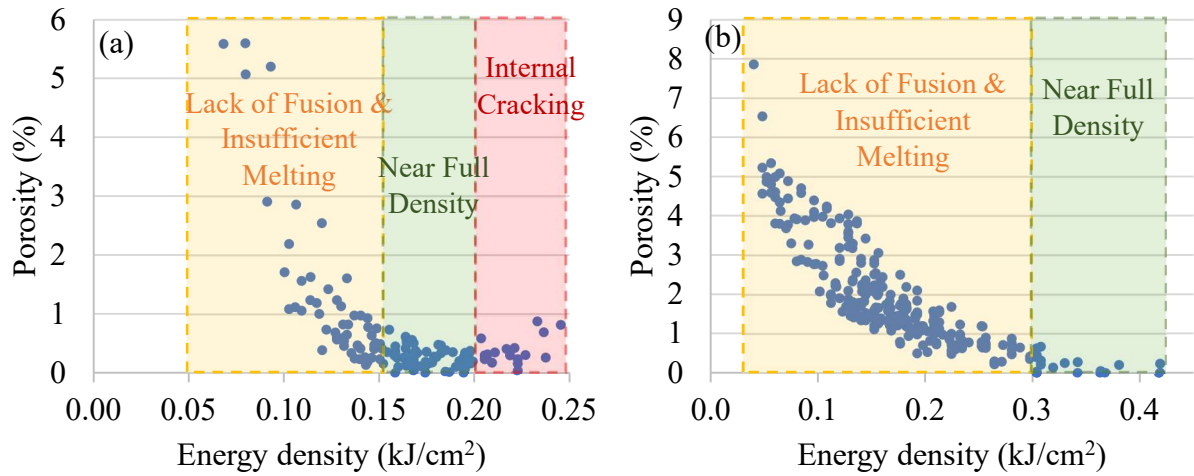


Figure 3. Relative porosity of (a) IN718 and (b) M300 vs. energy density of the diode laser per area.

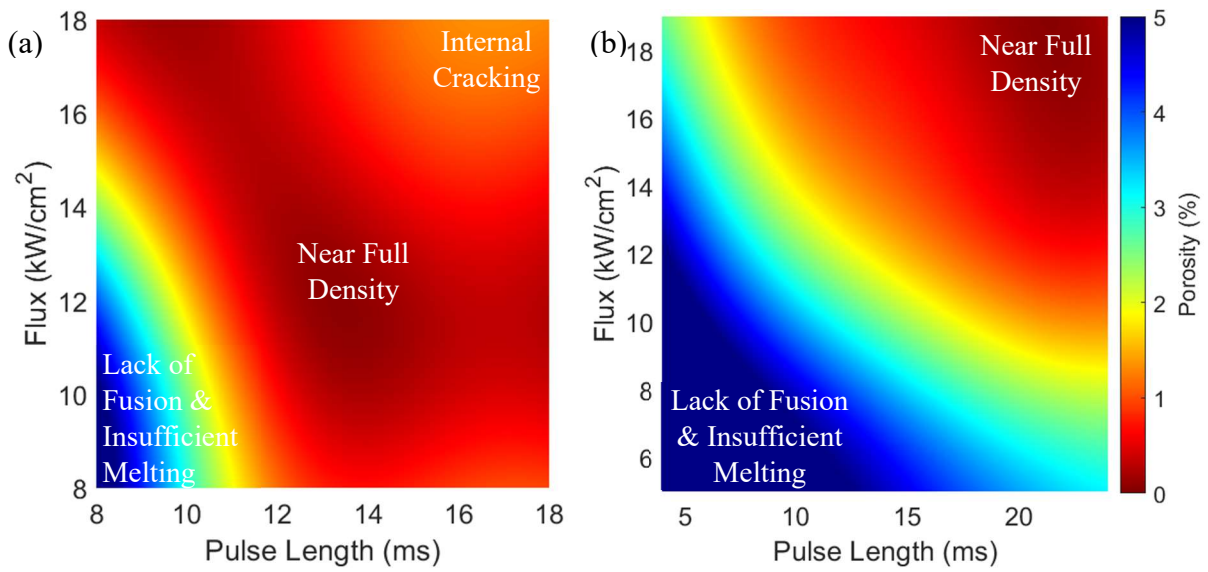


Figure 4. Surface plots of porosity vs. diode laser flux and pulse length for (a) IN718 and (b) M300.

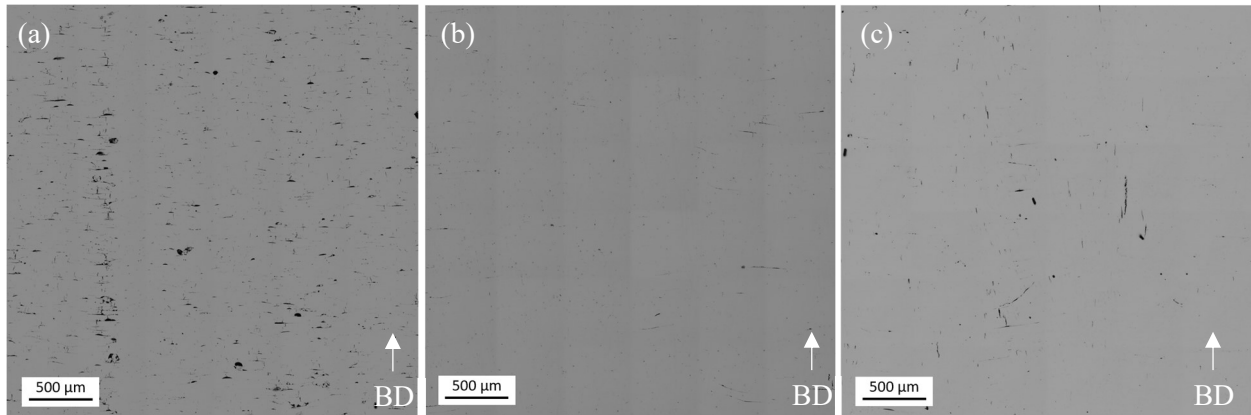


Figure 5. Micrographs of representative IN718 samples from different regions of the porosity vs. energy density plot: (a) low energy density showing lack of fusion and insufficient melting defects, (b) medium/high energy density resulting in near full density, and (c) very high energy density showing internal cracking as the dominant type of defect.

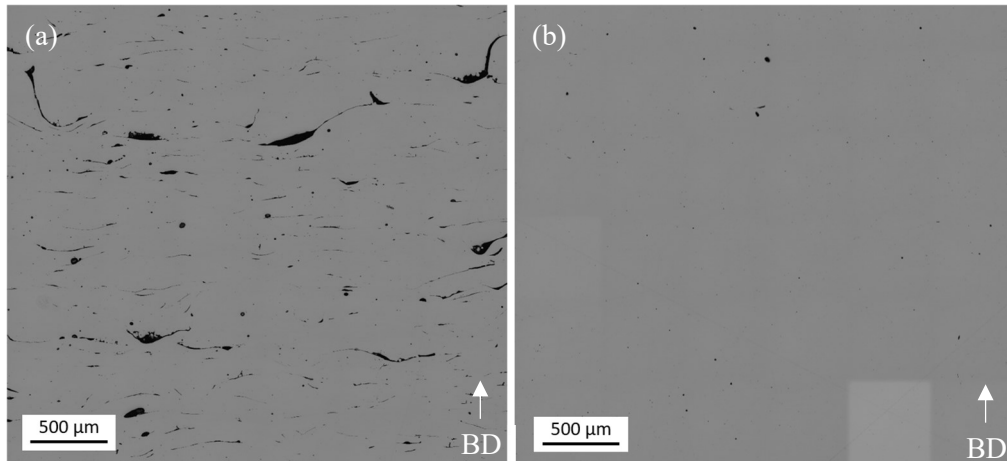


Figure 6. Micrographs of representative M300 maraging steel samples from different regions of the porosity vs. energy density plot: (a) low energy density showing lack of fusion and insufficient melting defects and (b) high energy density resulting in near full density.

Due to the nature of the Area Printing™ process, high-aspect-ratio melt pools are formed that are significantly wider and relatively shallower than the ones generally formed during the LPBF process. During the solidification process, cells grow epitaxially and perpendicular to melt pool boundaries [24]. As a result, in the case of having flat and horizontal melt pool boundaries for most of the part cross-section area, the favorable growth direction for most of the cells would be along the build direction. The melt pool width of a full tile in the Area Printing™ process is more than 100 times larger than its depth, which makes the resultant microstructures of Area Printed™ parts highly directional along the build direction, as illustrated in Figure 7 for M300 maraging steel.

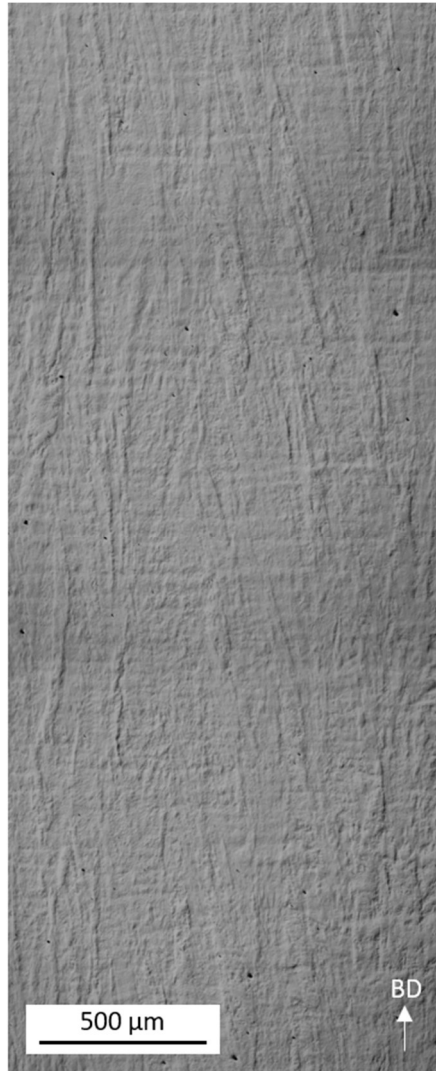


Figure 7. A representative M300 maraging steel polished cross-section showing epitaxially grown, highly directional grains extending along the build direction and planar melt pool boundaries orthogonal to the build direction.

3.1.2. Effect of Sample Size and Geometry on Density

It is shown in the literature that the size and geometry of LPBF-manufactured parts may have an influence on the parts' properties [25]. To investigate this effect on the density of IN718 samples, cubes and cylinders were fabricated with different sizes but with the same laser parameters. The size of the samples ranges from 3 mm to 14 mm. Figure 8 shows these samples on a prototype machine's build plate. The laser parameters were chosen to have a high porosity to make the differences in density more pronounced. Figure 9 shows the porosity variations for samples with different shapes and geometries. The results suggest that smaller parts have significantly higher porosity; In other words, porosity is decreased by increasing the sample size. The trend then reaches a steady state for features bigger than ~ 2.5 mm. As the dominant cooling mechanism for samples is conduction through the solid material to the build platform, decreasing the sample size results in a decrease in the cooling rates. So, a reason for the increase in porosity

by decreasing the sample size can be attributed to the accumulated heat in these samples due to slower cooling rates that can cause internal cracking in IN718 material, as discussed in section 3.1.1. Therefore, in parts with complex geometries, different parameter sets can be used for regions with small features. Also, slightly higher porosity was observed for cubes of different sizes compared to cylinders, which can be attributed to cylinders having a more efficient cross section to dissipate the heat from the top layer to the build platform.

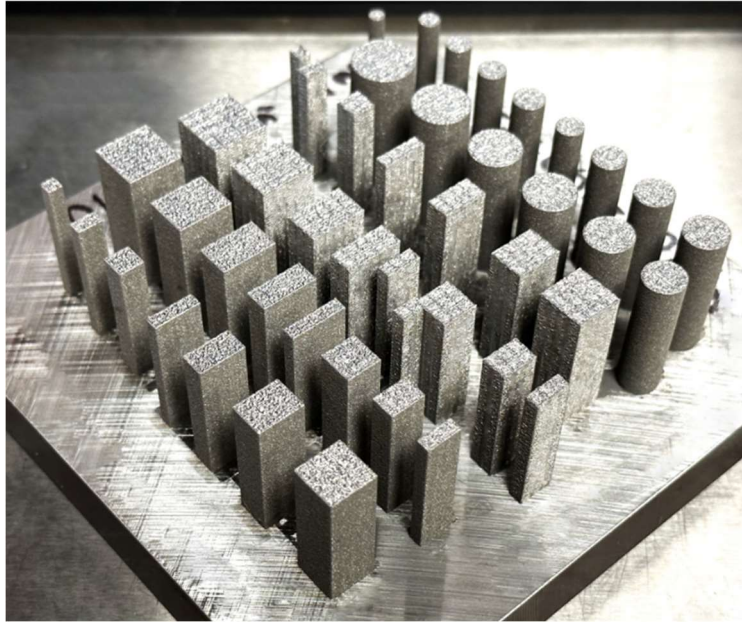


Figure 8. IN718 samples with different sizes and geometries (the two top rows and the two bottom rows were used for this study).

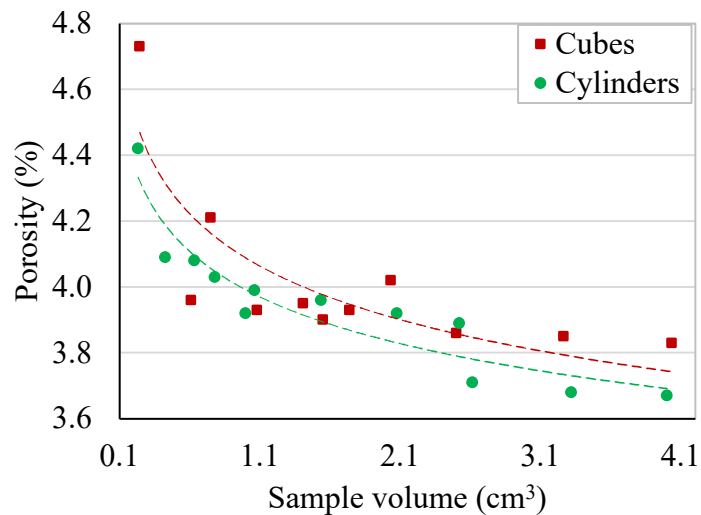


Figure 9. Effect of sample size on porosity in IN718.

3.1.3. Effect of In-situ Laser Shock Peening and Tile Overlap on Density

According to the literature, laser shock peening (LSP) improves the surface quality of additively manufactured parts [26,27]. Therefore, an extra shot of the laser was applied after the solidification of each tile to improve the surface roughness of each layer and, thus, to have a more uniform layer interface and enhanced bonding. Figure 10 shows an improvement in the relative density of IN718 parts at different energy levels using the in-situ LSP strategy. Tile overlap is another variable that influences the density of the Area Printed parts. Figure 11 shows this effect is more pronounced at higher laser powers.

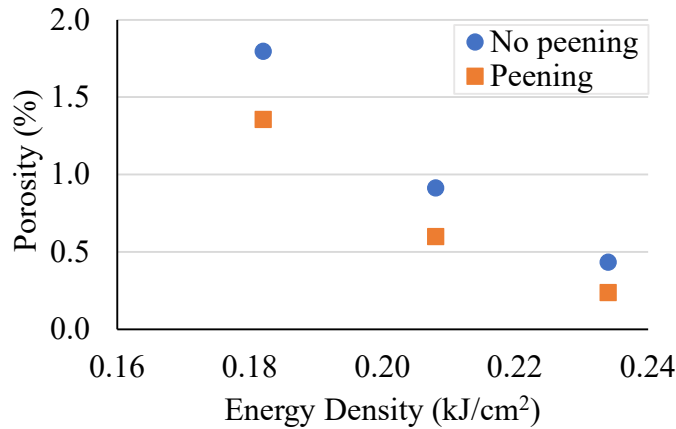


Figure 10. Effect of in-situ laser shock peening on porosity of IN718 parts.

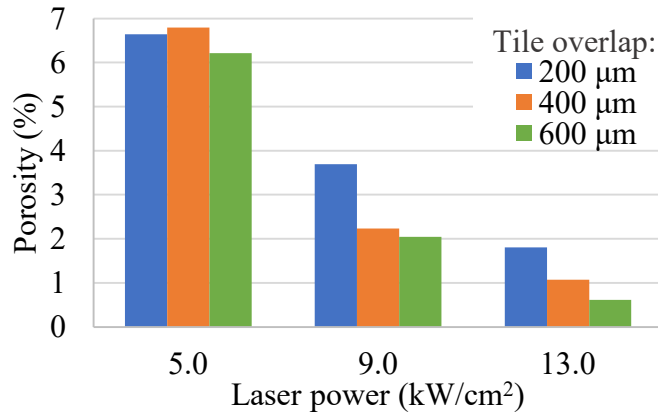


Figure 11. Effect of tile overlap on porosity of M300 maraging steel parts.

3.2. Simulation results

The simulation was set up to understand the melting and solidification behavior of the LAPBF process. Since the simulation model was designed with very small meshes, laser pulse length transformation is applied based on analytical expression to approximate the diode energy densities. To compare similar melting behavior at different laser parameters, $P \times \sqrt{t}$ can be used

as a constant for pulsed laser systems where P is laser power, and t is the pulse length [28]. This enables lowering the pulse length significantly, thus lowering the simulation time.

The simulation was carried out with a diode laser with approximate energy densities of $\sim 0.09 \text{ kJ/cm}^2$ and $\sim 0.18 \text{ kJ/cm}^2$ and YAG laser with $\sim 30 \text{ J/cm}^2$, 10 ns – 100 μs [pulse length Seurat proprietary]. The diode power was increased to 50 kW for the simulation, which lowered the pulse lengths to 0.5 ms and 1 ms, respectively. Figure 12 shows the state of the powder bed before the laser hits the powder bed. At low diode energy densities, some powder particles were partially melted. As the diode energy was increased to $\sim 0.18 \text{ kJ/cm}^2$, more powder particles were melted, and particle sintering and balling were dominant.

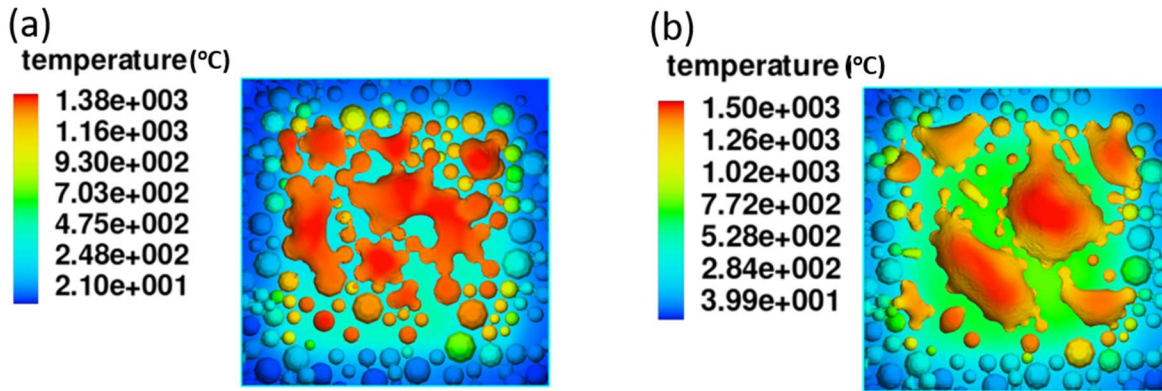


Figure 12. Temperature distribution and powder sintering at the end of the diode laser heating with (a) 0.09 kJ/cm^2 and (b) 0.18 kJ/cm^2 .

The YAG laser is applied to melt the powder layer completely. However, depending on the diode energy, the melted powder layer may or may not fuse to the substrate. Figure 13 presents the cross-sectional view of the melt pool at the end of the YAG laser for low energy diode. The applied lasers result in a high aspect ratio melt pool, and with a low energy diode, insufficient melting was observed, leading to high porosity. The melting and solidification with the YAG laser have also been discussed in previous work [29].

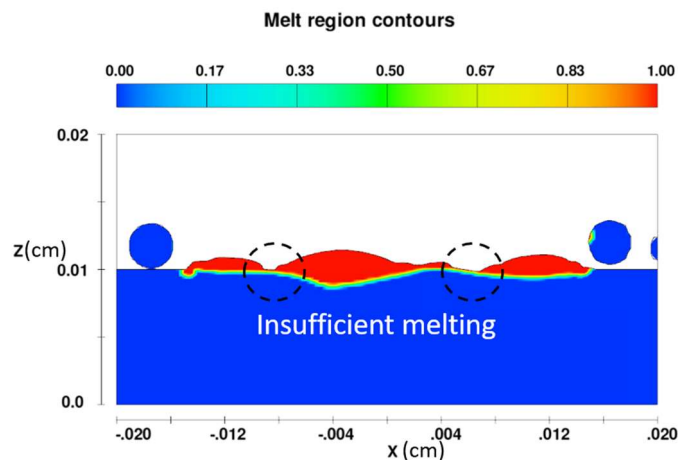


Figure 13. Melt region at the end of the YAG laser applied after low energy diode in IN718.

4. Conclusions

In this study, large-area pulsed laser powder bed fusion parameters are optimized to achieve near-full-density parts (>99.9 % relative density) using Ni-based super alloy 718 and M300 maraging steel. It is observed that the full-density area for IN718 is significantly narrower than that of M300. This is attributed to IN718 being prone to internal cracking at high energy densities because of the fast solidification and cyclic heating process. No inflection point was observed in the density plot of M300 samples by increasing the applied energy density. More experiments at higher energy densities and comparing the fully dense samples at various energies are yet to be carried out. Also, a computational model is developed to understand the multi-physics governing the process. The simulation results showed that increasing the diode laser power raises the powder bed temperature and, as a result, increases the size of the melt region. The higher temperatures and larger melt regions ensure proper inter-layer bonding when applying the YAG laser. Also, it is observed that the shallow depth and high aspect ratio of the melt pool lead to a unidirectional solidification front extending along the build direction where grains grow epitaxially, and highly directional microstructures are created.

References:

- [1] J. Li, J. Hu, Y. Zhu, X. Yu, M. Yu, H. Yang, Surface roughness control of root analogue dental implants fabricated using selective laser melting, *Addit Manuf.* 34 (2020) 101283. <https://doi.org/10.1016/J.ADDMA.2020.101283>.
- [2] S. Torres-Carrillo, H.R. Siller, C. Vila, C. López, C.A. Rodríguez, Environmental analysis of selective laser melting in the manufacturing of aeronautical turbine blades, *J Clean Prod.* 246 (2020) 119068. <https://doi.org/10.1016/J.JCLEPRO.2019.119068>.
- [3] Z. Sajedi, R. Casati, M.C. Poletti, M. Skalon, M. Vedani, Thermal fatigue testing of laser powder bed fusion (L-PBF) processed AlSi7Mg alloy in presence of a quasi-static tensile load, *Materials Science and Engineering: A.* 789 (2020) 139617. <https://doi.org/10.1016/J.MSEA.2020.139617>.
- [4] L. Zhang, B. Song, J.J. Fu, S.S. Wei, L. Yang, C.Z. Yan, H. Li, L. Gao, Y.S. Shi, Topology-optimized lattice structures with simultaneously high stiffness and light weight fabricated by selective laser melting: Design, manufacturing and characterization, *J Manuf Process.* 56 (2020) 1166–1177. <https://doi.org/10.1016/J.JMAPRO.2020.06.005>.
- [5] M. Mehrpouya, A. Vosooghnia, A. Dehghanghadikolaei, B. Fotovvati, The benefits of additive manufacturing for sustainable design and production, *Sustainable Manufacturing.* (2021) 29–59. <https://doi.org/10.1016/B978-0-12-818115-7.00009-2>.
- [6] P. Kumar, J. Farah, J. Akram, C. Teng, J. Ginn, M. Misra, Influence of laser processing parameters on porosity in Inconel 718 during additive manufacturing, *International Journal of Advanced Manufacturing Technology.* 103 (2019) 1497–1507. <https://doi.org/10.1007/S00170-019-03655-9/METRICS>.

- [7] B.B. Ravichander, A. Amerinatanzi, N.S. Moghaddam, Study on the Effect of Powder-Bed Fusion Process Parameters on the Quality of as-Built IN718 Parts Using Response Surface Methodology, *Metals* 2020, Vol. 10, Page 1180. 10 (2020) 1180. <https://doi.org/10.3390/MET10091180>.
- [8] W. Wang, S. Wang, X. Zhang, F. Chen, Y. Xu, Y. Tian, Process parameter optimization for selective laser melting of Inconel 718 superalloy and the effects of subsequent heat treatment on the microstructural evolution and mechanical properties, *J Manuf Process.* 64 (2021) 530–543. <https://doi.org/10.1016/j.jmapro.2021.02.004>.
- [9] S.Y. Liu, H.Q. Li, C.X. Qin, R. Zong, X.Y. Fang, The effect of energy density on texture and mechanical anisotropy in selective laser melted Inconel 718, *Mater Des.* 191 (2020) 108642. <https://doi.org/10.1016/J.MATDES.2020.108642>.
- [10] K. Georgilas, R.H.U. Khan, M.E. Kartal, The influence of pulsed laser powder bed fusion process parameters on Inconel 718 material properties, *Materials Science and Engineering: A.* 769 (2020) 138527. <https://doi.org/10.1016/J.MSEA.2019.138527>.
- [11] E.A. Jäggle, P.P. Choi, J. Van Humbeeck, D. Raabe, Precipitation and austenite reversion behavior of a maraging steel produced by selective laser melting, *J Mater Res.* 29 (2014) 2072–2079. <https://doi.org/10.1557/JMR.2014.204>.
- [12] G. Casalino, S.L. Campanelli, N. Contuzzi, A.D. Ludovico, Experimental investigation and statistical optimisation of the selective laser melting process of a maraging steel, *Opt Laser Technol.* 65 (2015) 151–158. <https://doi.org/10.1016/J.OPTLASTEC.2014.07.021>.
- [13] M. Król, P. Snopiński, J. Hajnyš, M. Pagáč, D. Łukowiec, Selective Laser Melting of 18Ni-300 Maraging Steel, *Materials* 2020, Vol. 13, Page 4268. 13 (2020) 4268. <https://doi.org/10.3390/MA13194268>.
- [14] Z. Mao, X. Lu, H. Yang, X. Niu, L. Zhang, X. Xie, Processing optimization, microstructure, mechanical properties and nanoprecipitation behavior of 18Ni300 maraging steel in selective laser melting, *Materials Science and Engineering: A.* 830 (2022) 142334. <https://doi.org/10.1016/J.MSEA.2021.142334>.
- [15] J. Vishwakarma, K. Chattopadhyay, N.C. Santhi Srinivas, Effect of build orientation on microstructure and tensile behaviour of selectively laser melted M300 maraging steel, *Materials Science and Engineering A.* 798 (2020). <https://doi.org/10.1016/j.msea.2020.140130>.
- [16] <https://www.seurat.com/area-printing>, (n.d.).
- [17] C. Kloss, C. Goniva, A. Hager, S. Amberger, S. Pirker, Models, algorithms and validation for opensource DEM and CFD-DEM, *Progress in Computational Fluid Dynamics.* 12 (2012) 140–152. <https://doi.org/10.1504/PCFD.2012.047457>.
- [18] S. Shrestha, Y. Kevin Chou, A Numerical Study on the Keyhole Formation During Laser Powder Bed Fusion Process, *J Manuf Sci Eng.* 141 (2019). <https://doi.org/10.1115/1.4044100>.
- [19] B. Fotovvati, K. Chou, Multi-layer thermo-fluid modeling of powder bed fusion (PBF) process, *J Manuf Process.* 83 (2022) 203–211. <https://doi.org/10.1016/J.JMAPRO.2022.09.003>.

- [20] K.C. Mills, Recommended Values of Thermophysical Properties for Selected Commercial Alloys, Woodhead Publishing Limited, Cambridge, England, n.d.
<https://books.google.com/books?hl=en&lr=&id=GaOooR231aAC&oi=fnd&pg=PR7&ots=WmPCRequuz&sig=99F2BLqybZGkONPd91WBZaTnr6s#v=onepage&q&f=false> (accessed May 14, 2023).
- [21] K. Georgilas, R.H.U. Khan, M.E. Kartal, The influence of pulsed laser powder bed fusion process parameters on Inconel 718 material properties, *Materials Science and Engineering: A*. 769 (2020) 138527. <https://doi.org/10.1016/J.MSEA.2019.138527>.
- [22] W.Y. Chen, X. Zhang, M. Li, R. Xu, C. Zhao, T. Sun, Laser powder bed fusion of Inconel 718 on 316 stainless steel, *Addit Manuf.* 36 (2020). <https://doi.org/10.1016/j.addma.2020.101500>.
- [23] Y. Chen, F. Lu, K. Zhang, P. Nie, S.R. Elmi Hosseini, K. Feng, Z. Li, Dendritic microstructure and hot cracking of laser additive manufactured Inconel 718 under improved base cooling, *J Alloys Compd.* 670 (2016) 312–321. <https://doi.org/10.1016/J.JALLCOM.2016.01.250>.
- [24] M.S. Pham, B. Dovggy, P.A. Hooper, C.M. Gourlay, A. Piglione, The role of side-branching in microstructure development in laser powder-bed fusion, *Nature Communications* 2020 11:1. 11 (2020) 1–12. <https://doi.org/10.1038/s41467-020-14453-3>.
- [25] B. Fotovvati, E. Asadi, Size effects on geometrical accuracy for additive manufacturing of Ti-6Al-4V ELI parts, *International Journal of Advanced Manufacturing Technology*. 104 (2019) 2951–2959. <https://doi.org/10.1007/S00170-019-04184-1/METRICS>.
- [26] E. Maleki, S. Bagherifard, O. Unal, M. Bandini, M. Guagliano, On the effects of laser shock peening on fatigue behavior of V-notched AlSi10Mg manufactured by laser powder bed fusion, *Int J Fatigue*. 163 (2022) 107035. <https://doi.org/10.1016/J.IJFATIGUE.2022.107035>.
- [27] I. Yeo, S. Bae, A. Amanov, S. Jeong, Effect of Laser Shock Peening on Properties of Heat-Treated Ti-6Al-4V Manufactured by Laser Powder Bed Fusion, *International Journal of Precision Engineering and Manufacturing - Green Technology*. 8 (2021) 1137–1150. <https://doi.org/10.1007/S40684-020-00234-2/METRICS>.
- [28] W.E. King, H.D. Barth, V.M. Castillo, G.F. Gallegos, J.W. Gibbs, D.E. Hahn, C. Kamath, A.M. Rubenchik, Observation of keyhole-mode laser melting in laser powder-bed fusion additive manufacturing, *J Mater Process Technol.* 214 (2014) 2915–2925. <https://doi.org/10.1016/J.JMATPROTEC.2014.06.005>.
- [29] J.D. Roehling, S.A. Khairallah, Y. Shen, A. Bayramian, C.D. Boley, A.M. Rubenchik, J. DeMuth, N. Duanmu, M.J. Matthews, Physics of large-area pulsed laser powder bed fusion, *Addit Manuf.* 46 (2021) 102186. <https://doi.org/10.1016/J.ADDMA.2021.102186>.